

The Influence of Temperature on Oxide-Scale Formation during Erosion–Corrosion

Rikard Norling and Anders Nylund*

Received May 21, 2004; revised November 1, 2004

Four steels (Fe2.25Cr1Mo, Fe9Cr1Mo, AISI 304, 353 MA) and one Ni-based superalloy (Inconel 625) were exposed in an erosion–corrosion test rig at the temperatures 20, 350, 550 and 700°C for 1 week. The atmosphere was air and the particle velocity 1.2 m/s. The composition and thickness of the developed surface layers were determined by Auger electron spectroscopy and X-ray photoelectron spectroscopy. The ferritic and Ni-based alloys investigated show a minimum in wastage rate around 350°C due to the development of a particle strengthened/toughened composite layer on the surface. The greatest wastage rates were measured at 700°C. Rapid diffusion paths created in the oxide from the particle bombardment results in the growth of oxide nodules at the oxide/metal-interface causing protruding oxide flakes which are chipped away. At this temperature the ferritic steel Fe9Cr1Mo is degraded to a larger extent than the austenitic steels.

KEY WORDS: erosion–corrosion; surface analysis; AES; XPS; particle strengthening.

INTRODUCTION

The economical and environmental benefits of fluidized bed combustion (FBC) technology have significantly increased its importance for production of heat and electricity. However, the technique has the drawback that components such as the combustion chamber walls and superheater tubes are subjected to erosion–corrosion phenomena. Especially susceptible are

Materials Science and Engineering, Chalmers University of Technology, SE-412 96 Göteborg, Sweden.

*To whom correspondence should be sent. Tel.: +46-31-7721263; Fax: +46-31-7721262; E-mail: anders.nylund@me.chalmers.se

plants operating on biomass,¹ but problems are also encountered in traditional coal-fired systems.²

Understanding of the erosion-corrosion phenomenon is usually based on characterizing it in different regimes, each being characterized by its own surface morphology based on the erosive and corrosive mechanisms taking place. In the literature the number of regimes has been suggested to be three,³⁻⁵ four^{6,7} or six.^{8,9} The most widespread alternative is the one elaborated by Rishel *et al.*,⁹ in which the following regimes are proposed in order of increasing erosion rate and decreasing corrosion rate: erosion of oxide only; erosion-enhanced corrosion type II, type I and type III; oxidation-affected erosion; and erosion of metal only. All three types of erosion-enhanced corrosion have in common that only the oxide scale is eroded and the metal recession is increased by the impacting particles (compared to what it would have been for corrosion only). In type I the oxide scale becomes thinner due to the erosive wear. The shorter diffusion paths for the reacting species then increase the rate of material degradation. Type II differs from type I in that erosion modifies the oxide scale in such a way that the transfer rate of reactive species from the atmosphere to the oxide/metal interface is increased independent of the scale thickness. Type III appears when erosion, promotes spalling of the oxide scale. During oxidation-affected erosion, the erosion rate exceeds the corrosion rate to such an extent that not only the oxide scale but also the underlying metal is directly eroded. A composite layer consisting of corrosion products, base metal and incorporated erodent material is formed.

A change in erosion-corrosion regime and thereby in most cases also wastage rate occurs when the temperature or particle velocity is varied substantially, although other factors, such as the alloy and gas compositions and type of erodent material, have an influence as well. Throughout the years a number of studies have been performed to evaluate how the temperature influences the wastage rate. The results are often contradictory. The wastage rate as a function of increasing temperature has been reported as: increasing;^{9,10} decreasing;¹⁰ increasing followed by a decreasing rate;^{11,12} increasing followed by a decreasing rate and then a drastic increase;¹³ constant rate followed by a sudden drop and then a drastic increase.¹⁴ Though in some cases the discrepancy between the graphs can be explained by too few or too sparsely distributed exposure temperatures, it is clear that a general relationship between the temperature and wastage rate is hard to predict. It must also be taken into consideration that the temperature dependence might differ among various materials due to their individual oxidation properties.

The erosion-corrosion wastage rate of a metal surface is governed by the degradation mechanisms taking place during exposure to an erosive

environment. Their accurate determination requires detailed information on how the surface properties are coupled to the changes in erosion–corrosion regime for the system in question. The aim of this work is therefore to study the influence of temperature on the scale formation in terms of surface chemistry and morphology during erosion–corrosion of iron and nickel-based alloys.

EXPERIMENTAL METHODS

Exposures

The erosion–corrosion exposures were performed in a test rig as illustrated in Fig. 1. In the test rig up to 5 samples positioned parallel to each other can be exposed to a hot gas stream entraining erodent particles. The particles are preheated in a fluidized bed located in the upper part of the furnace, extracted through a nozzle and blown onto the mid-points of the rectangular samples. The sample ends are protected from the particle stream and are used as reference areas when determining the erosive wear and oxidation behavior during gas load only. The particles are continuously recycled and fed back to the bed. In order to prevent pre-oxidation of the samples at the test start-up they are inserted directly from the cooling chamber into the hot furnace and immediately exposed to the erodent stream. The exposures are interrupted instantaneously by

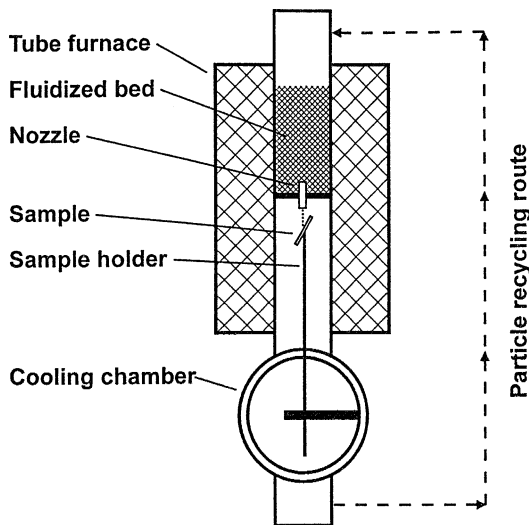


Fig. 1. The erosion–corrosion test rig.

Table I. Alloy compositions (wt.%)

Alloy	C	Si	Mn	Cr	Ni	Mo	Fe	Others	Structure
Fe-2.25Cr-1Mo	0.10	0.24	0.47	2.21	—	0.99	balance	—	Ferrite
Fe-9Cr-1Mo	0.10	0.39	0.44	8.7	0.27	0.95	balance	0.22 V 0.07 Nb	Ferrite
AISI 304	0.027	0.55	1.41	18.46	10.19	0.49	balance	—	Austenite
353 MA	0.052	1.70	1.43	24.9	34.2	0.13	balance	0.17 N 0.06 Ce	Austenite
Inconel 625	0.016	0.03	0.35	21.75	balance	9.41	0.09	3.47 (Nb + Ta)	Austenite

dropping the sample holder into the cooling chamber below and shutting off the erodent stream. The cooling rate is further increased by blowing cold N₂ gas directly onto the samples. Thereby the oxide condition at high temperature is conserved for analysis. A detailed description of the test rig is given elsewhere.¹⁵

The samples were exposed to the test temperatures 20, 350, 550 and 700°C and the exposure time was 168 hr. The exposures at elevated temperature were repeated twice. The oxidizing gas was pressurized air dried to a dew point of −30°C. Angular alumina particles with a diameter of 250–300 μm were utilized as erodent material. The impact angle, defined as the angle between the sample surface and the erodent stream, was 30°. The particle velocity at room temperature was 2.0 ± 0.3 m/s and at elevated temperatures 1.2 ± 0.3 m/s. Due to the nozzle construction the mass flow of the erodent varied with temperature. The mass flows were measured to be 8.3 ± 1.2, 2.4 ± 0.8, 2.3 ± 0.4 and 4.1 ± 0.9 g/s, given in order of increasing temperature.

The materials investigated were two ferritic and two austenitic steels and one nickel-based superalloy. They are all commercial grades and their compositions are given in Table I. The sample pre-treatment procedure was grinding on emery paper and polishing with 7 μm diamond paste.

Analysis Techniques

The erosion–corrosion degradation was determined by recording surface topography profiles over the samples using stylus profilometry (Mitutoyo SV-502). From the topography profiles the erosive wear was taken as the depth of the hollow at the sample mid-points, with the non-eroded sample ends as references.

The oxide compositions and thicknesses were determined using depth profiling with Auger electron spectroscopy (AES, PHI 660). The electron acceleration voltage and beam current were 10 kV and 100 nA, respectively, giving a lateral resolution of about 1 μm. Each analysis was made as a set of several spot-analyses in the area of interest. The depth profiles were obtained by intermittent analysis during ion etching with Ar⁺. The oxide

thicknesses were then taken as the etch depth at which the oxygen signal decreased to its half maximum value. The ion beam accelerating voltages used were in the range 1.5–4.0 kV and the beam was rastered over an area of 1 mm \times 1 mm. The etch rates were determined by depth profiling on Ta₂O₅ layers of known thickness.

The atomic concentrations were determined from peak-to-peak intensities in the differentiated spectra utilizing sensitivity factors provided by the instrument manufacturer for pure elements. The overlap problem between the Cr(LMM) and O(KLL) peaks was dealt with by using only the high kinetic energy side of the Cr(LMM) peak and scaling the sensitivity factor for Cr accordingly. This technique has been described in detail previously.¹⁶ The use of sensitivity factors determined for pure elements when evaluating oxides introduces some discrepancies in the concentration profiles, especially concerning the oxygen level. However, the error in the ratio between the cation concentrations is small as the relative differences in the sensitivity factors are minor.¹⁶ Thus, the depth profiles for the cations can be compared directly.

X-ray photoelectron spectroscopy (XPS, PHI 5500, monochromized AlK _{α} X-ray source) was used on some samples to obtain depth profiles with detailed information on the chemical state of the oxide constituents. The binding energy, BE, scale of the instrument was calibrated on Au and Cu samples (Au 4f_{7/2}: BE = 84.0 eV; Cu 2p_{3/2}: BE = 932.7 eV). The take-off angle (defined as the angle between the sample surface and the spectrometer entrance) of the photoelectrons was 45° and the spectrometer was operated at a pass energy of 46.95 eV. The diameter of the analyzed area was about 0.8 mm. The depth profiles were obtained by Ar ion etching at a beam voltage of 4 kV and with a raster size of 3 mm \times 3 mm. The etch rates were obtained in a manner similar to that described above for the AES analysis.

The XPS quantification was performed under the assumption that the analyzed volume consists of a mixture of oxide and/or metal grains, each being homogeneous and having a grain size larger than $3\lambda_{X,i}$, where $\lambda_{X,i}$ is the photoelectron attenuation length for the analyzed element. This assumption allows for the same simplification of the intensity expressions as when analyzing (contamination and surface oxide free) bulk materials or thick (larger than $3\lambda_{X,i}$) homogeneous layers covering the whole analyzed surface. The measured photoelectron intensity for the i th level of species X, $I_{X,i}$, then becomes

$$I_{X,i} = k_s I_{hv} A_{\Theta} Y_{X,i} D_X \lambda_{X,i} \sin \Theta$$

where I_{hv} is the X-ray intensity on the sample surface, A_{Θ} is the analyzed area, k_s is a factor taking into account the current condition of

Table II. Parameters used for quantitative XPS analysis (monochromized AlK_{α} , PHI 5500)

Signal	Compound	Density (mole/cm ³)	Yield factor (eV · ke · cm ³ /Å · s · mole)	λ (Å)
Al 2p _{3/2}	Al ₂ O ₃	0.078	1.6	22.5
O 1s	Al ₂ O ₃	0.117	10	17
Cr 2p _{3/2}	304 alloy	0.028	21.7	13.5
Cr 2p _{3/2}	Cr ₂ O ₃	0.069	23.8	16
O 1s	Cr ₂ O ₃	0.103	10	16.5
Fe 2p _{3/2}	304 alloy	0.097	24.8	12
Fe 2p _{3/2}	Fe ₂ O ₃	0.066	18	15
O 1s	Fe ₂ O ₃	0.098	10	16.5
Mo 3d _{5/2}	304 alloy	0.0004	19.1	17
Mo 3d _{5/2}	MoO ₃	0.033	23	21
O 1s	MoO ₃	0.098	10	17
Ni 2p _{3/2}	304 alloy	0.014	47.4 ^a	10
Ni 2p _{3/2}	NiO	0.089	49.6 ^a	13
O 1s	NiO	0.089	10	16.5

^aIncluding satellites.

the spectrometer and Θ is the take-off angle. $Y_{X,i}$ is an equipment dependent experimental photoelectron yield factor and D_X is the density of the element. The parameters used for the XPS quantifications are given in Table II.

SEM micrographs were recorded from the oxide surfaces by a scanning electron microscope (LEO Gemini 1550) equipped with a field emission gun. The instrument was operated at low voltage (5 kV) in the in-lens secondary electron detector mode to achieve high lateral resolution (<10 nm).

RESULTS

Wastage Rates

The metal recession due to erosion–corrosion has been determined for the various alloys up to 700°C. The data shown in Fig. 2, in terms of wastage rate (mm/1000 hr) vs. temperature, are the average values as calculated from the number of exposures performed at each temperature. In order to facilitate comparison between the temperatures and previously published data¹⁵ the wastage rates have been scaled to correspond to the mass flow and particle velocity at 550°C (2.3 g/s, 1.2 m/s). The scaling regarding the particle velocity was done according to the power law expression by Finnie with a velocity exponent of 2.4.^{17,18} The curves show a minimum in wastage rate around 350°C for the ferritic and Ni-based alloys. No data are given for the Fe2.25Cr1Mo steel at the temperature 550°C due to severe oxidation and

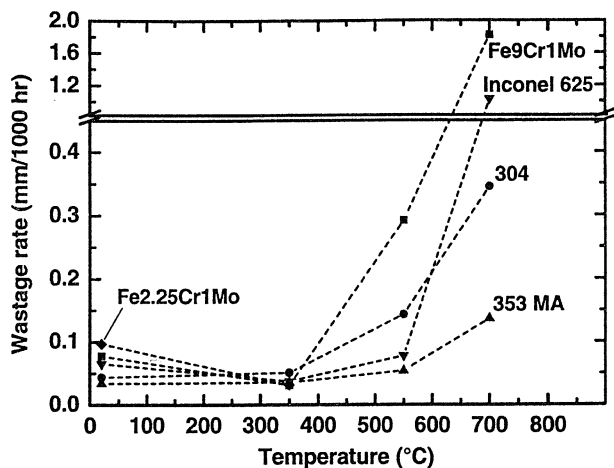


Fig. 2. Wastage rates during erosion-corrosion scaled to correspond to the mass flow and particle velocity at 550°C (2.3 g/s, 1.2 m/s).

spalling on the non-eroded reference surfaces. Nevertheless, a rough estimation of the erosion-corrosion wastage rate from the surface topography profile showed that it is close to what was measured on the Fe9Cr1Mo steel. When the temperature is changed from 550 to 700°C the wastage rates for the Fe9Cr1Mo steel and the Ni-based superalloy (Inconel 625) increase dramatically by factors of six and thirteen, respectively. On the other hand, the corresponding increase on the austenitic steels (AISI 304 and 353 MA) is only a factor of about two. The Fe2.25Cr1Mo alloy was excluded from the tests performed at 700°C.

Surface Layer Formation at 20°C

In Fig. 3a, b AES depth profiles recorded from 304 and Fe9Cr1Mo samples eroded at 20°C are shown. The thickness of the surface layer is about 1.3 μm . The low temperature excludes extensive oxidation. Instead fragments from the erodent alumina particles are incorporated into the metal phase. The SEM micrograph in Fig. 4a shows that a large number of alumina fragments are present on the surface of the 304 sample. A close-up of one fragment, fractured in the brittle mode, is given in Fig. 4b.

Oxide Formation at 350°C

The surface layers formed during erosion-corrosion at 350°C are rather similar for all the alloys investigated. The thickness is about 1–4 μm

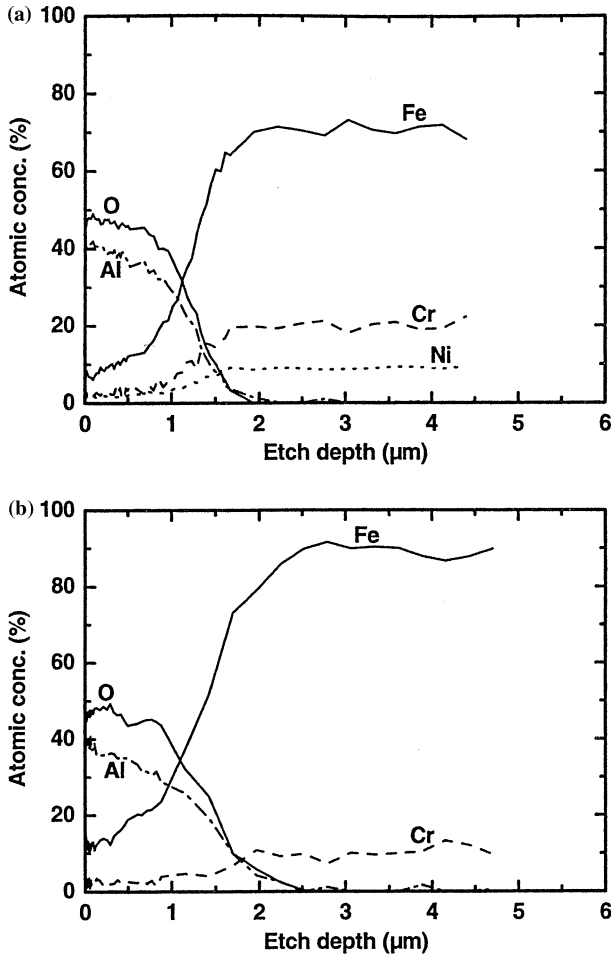


Fig. 3. AES depth profiles recorded from (a) a 304 sample and (b) an Fe9Cr1Mo sample eroded at 20°C.

and varies locally over the surface, as illustrated in Fig. 5a, b, which show AES depth profiles recorded from two neighboring analysis spots on an eroded 304 sample. It is seen that also after exposure at this temperature the surface layer consists mostly of incorporated erodent fragments. In Fig. 5c corresponding depth profiles from the sample area subjected to pure oxidation are shown. The difference is striking. Compared to the surface layer on the eroded area, the scale on the non-eroded part is only about one hundredth as thick. Alumina is not detected at all as this area

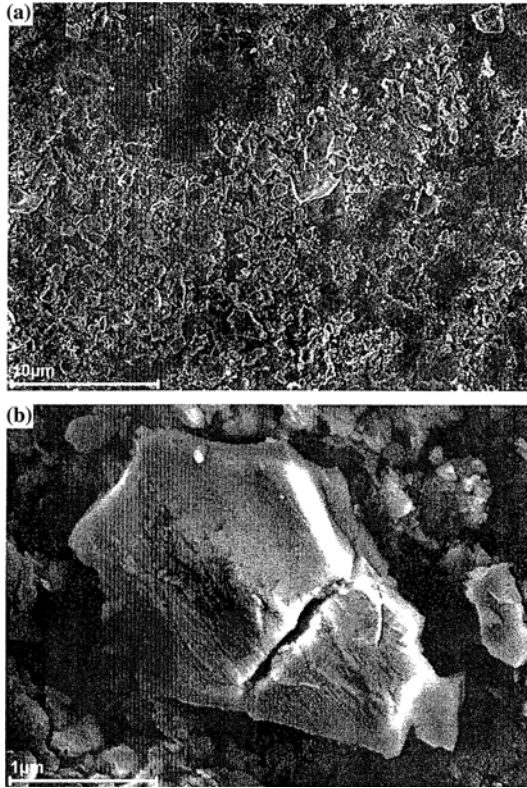


Fig. 4. SEM micrograph recorded from a 304 sample eroded at 20°C. (a) Overview of the surface layer, (b) close-up of a partially embedded fragment of the alumina erodent.

was not exposed to the erodent. Considering only the alloy constituents, there is another notable difference between them. If Al is excluded the eroded surface layer has a rather homogeneous composition, with Fe as the major cation element, while the non-eroded oxide displays a double-layered structure with one outer layer mainly consisting of Fe-oxide and one inner layer considerably enriched in Cr.

From the AES depth profiles presented in Fig. 5a, b, the chemical state of the recorded elements cannot be conclusively determined. This problem was overcome by performing XPS depth profiling. Figure 6a shows the XPS depth profiles obtained from a 304 sample eroded at 350°C, while Fig. 6b is simply a magnification of the lower left corner

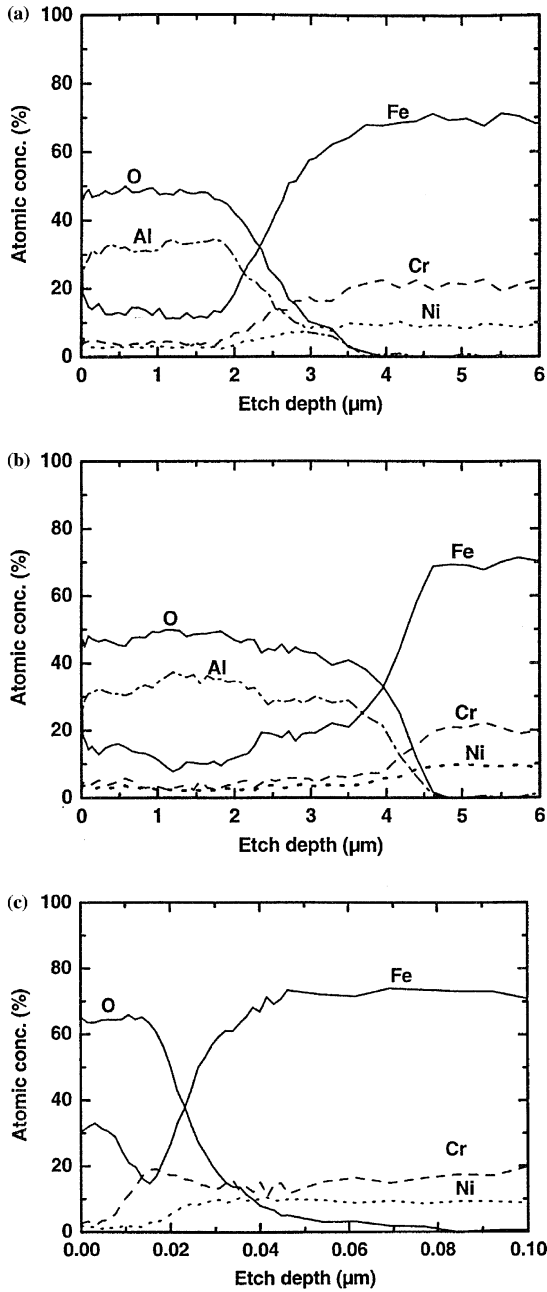


Fig. 5. AES depth profiles recorded from a 304 sample exposed at 350°C. (a) and (b) two neighboring analysis spots in the eroded area, (c) area subjected to pure oxidation.

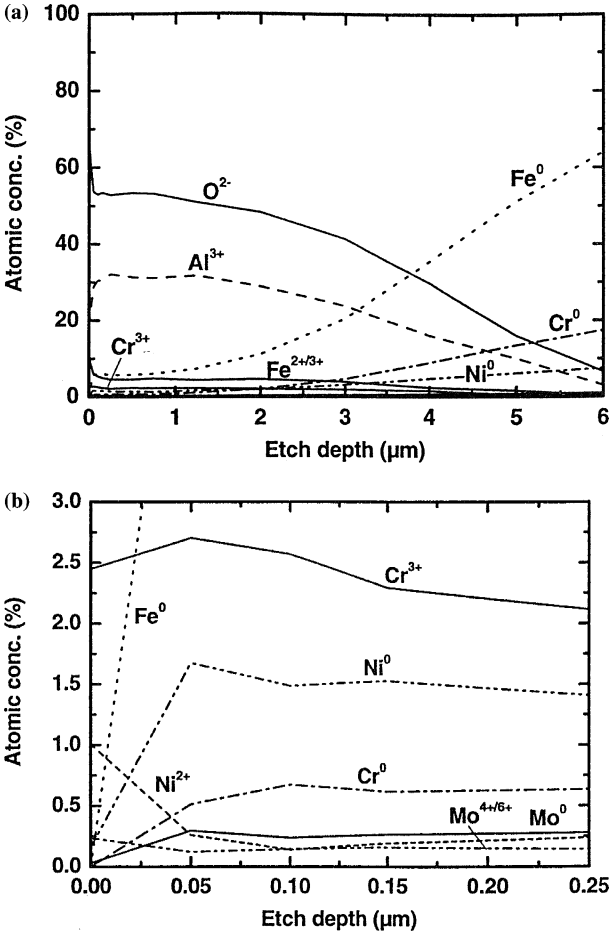


Fig. 6. XPS depth profiles recorded from a 304 sample eroded at 350°C. A close-up of the lower left-hand corner of (a) is given in (b).

in Fig. 6a. From the profiles it is clear that the surface has transformed into a composite structure of alumina fragments incorporated in a mixture of oxides and metal. The composition of the composite surface layer, down to an etch depth of about 1 μm, is approximately two thirds Al_2O_3 , one sixth (Fe,Cr) oxides and one sixth alloying elements in their metallic state. However, it is likely that part of the metallic Fe arises from reduction during the ion etching. Deeper into the composite surface layer the metal phase content increases. By summing the cation and metal state

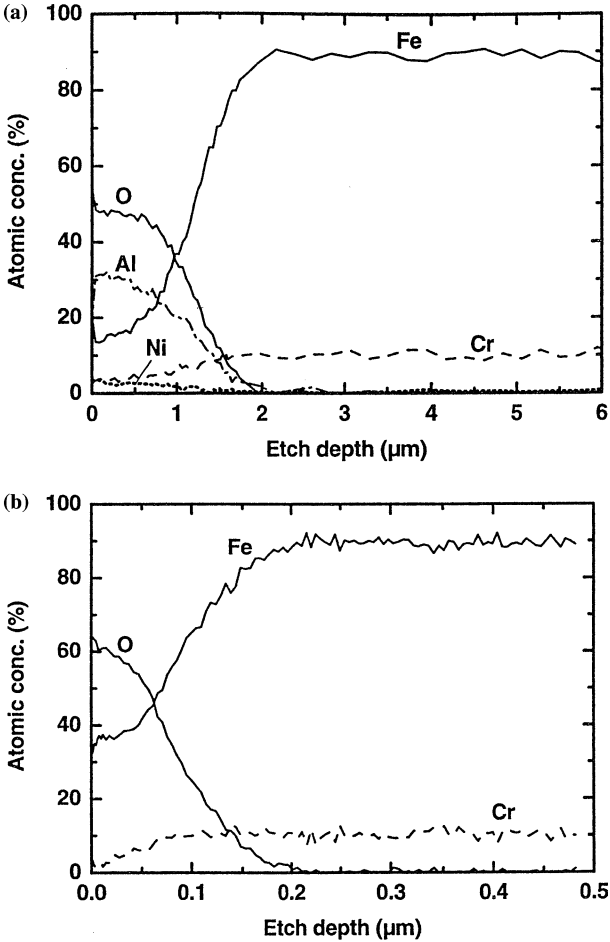


Fig. 7. AES depth profiles recorded from an Fe9Cr1Mo sample exposed at 350°C. (a) Eroded area, (b) area subjected to pure oxidation.

concentrations for each alloying element and calculating their proportions, it is seen that the composite surface layer composition in terms of the alloying elements is equal to that of the bulk material, independent of etch depth, with a determined error of less than 3%.

Figure 7a, b show AES depth profiles obtained from one eroded area and one area subjected to pure oxidation on an Fe9Cr1Mo sample exposed at 350°C. Also in this case, Al-oxide fragments have penetrated

the Fe/Cr-oxide on the eroded area. However, some Ni is found in the composite surface layer, despite the fact that Ni is only a trace element in the Fe9Cr1Mo alloy. It has been shown previously¹⁵ that this is due to contamination present on the surface of the erodent particles caused by wear of the stainless steel test rig. No Cr enrichment is found in the oxide on the non-eroded area and the scale thickness is only about $0.08\text{ }\mu\text{m}$, which is to be compared with the $1\text{--}4\text{ }\mu\text{m}$ for the eroded area.

The AES depth profiles recorded on an eroded 625 sample show that the surface is penetrated by alumina fragments in a similar way as for the 304 and Fe9Cr1Mo samples, Fig. 8a. In addition, the sample surface is covered with deposited Fe oxides as a result of contaminated erodent (see above). The oxide scale formed on the area exposed to pure oxidation is two layered, Fig. 8b, as on the 304 sample, but with an almost pure Ni-oxide on top of a Cr-enriched oxide.

Comparing the micrographs in Figs. 4a and 9 shows that the surface appearances of the 304 samples exposed at room temperature and 350°C differ markedly. The number of micrometer sized alumina fragments present at the surface is much lower at the higher temperature. In Fig. 10 an example of such fragments partly embedded in the surface of an Fe9Cr1Mo sample is shown. According to the detailed surface pattern observed in the micrograph the following scenario can be outlined; the impinging particle came in from above in the picture, hit the surface, cut a trajectory into the metal phase, bounced off, and left behind a few broken off fragments.

Oxide Formation at 550°C

Oxide formation during erosion–corrosion at 550°C was studied previously with the same experimental test rig.¹⁶ At this temperature both ferritic and austenitic steels form a $1\text{--}2\text{ }\mu\text{m}$ thick oxide scale with alumina fragments present only in the outer part. This is exemplified in Fig. 11 by the AES depth profiles recorded from a 304 sample eroded at 550°C . The corresponding surface structure is displayed in Fig. 12. A typical characteristic after exposure at this temperature is the high frequency of cracks in the scales developed on the investigated steel types.

XPS-analyses of samples exposed at 550°C have shown that the metal particle content in the oxide scales is considerably lower than during erosion–corrosion at 350°C . This is illustrated by the depth profiles in Fig. 13, which reveals that down to an etch depth of $0.5\text{ }\mu\text{m}$ the concentration of metallic Cr is below 0.3%. The presence of metallic Fe in the absence of metallic Cr in the outer part of the oxide is a strong indication that the metal phase detected is a result of the Ar ion etching. Also by summing

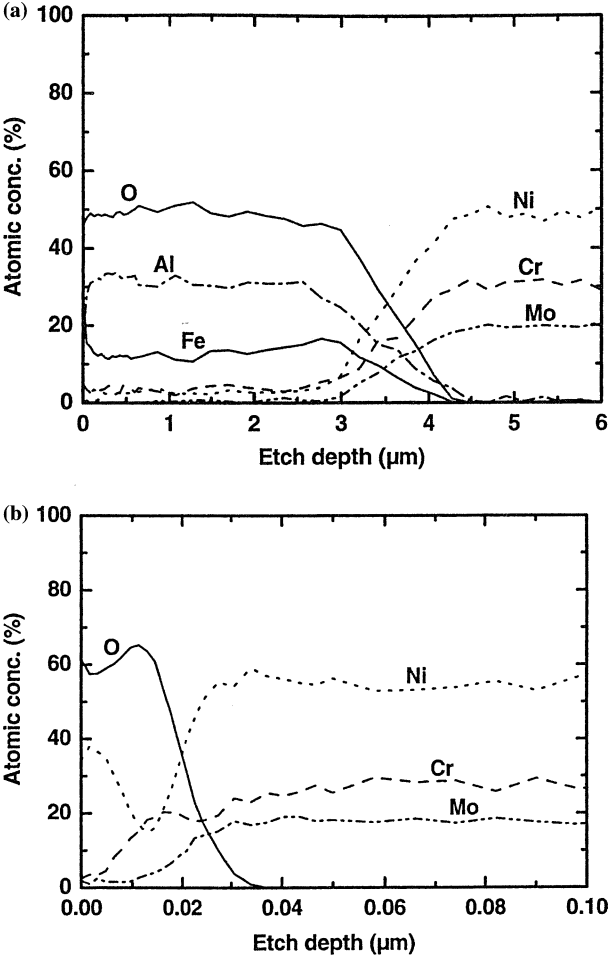


Fig. 8. AES depth profiles recorded on an Inconel 625 sample exposed at 350°C. (a) Eroded area, (b) area subjected to pure oxidation.

the cation and metal state contents for each alloying element at this temperature it is found, that the scale composition resembles the bulk material (with the same accuracy). This suggests that the erosion rate exceeds the diffusion rates of the alloying elements preventing any enrichment or depletion in the scale.

The composite surface layer composition on the Ni-based superalloy (Inconel 625) at 550°C is almost identical to that at 350°C. The major

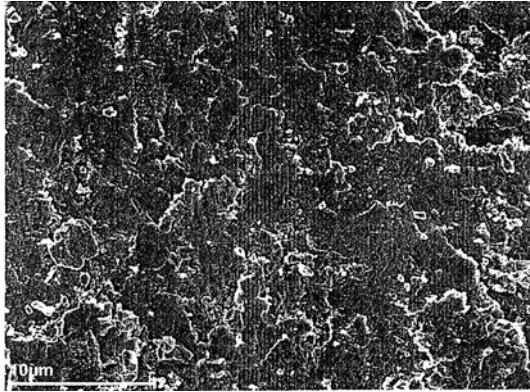


Fig. 9. SEM micrograph recorded from a 304 sample eroded at 350°C.

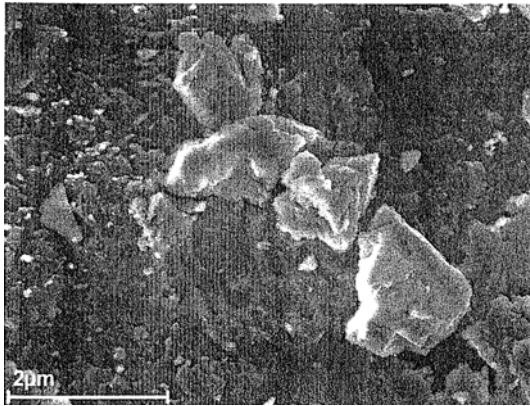


Fig. 10. SEM micrograph recorded from an Fe9Cr1Mo sample eroded at 350°C showing the impact site of an eroding particle.

difference is the somewhat thinner composite surface layer, which is about $1\text{ }\mu\text{m}$ at these temperatures.

Oxide Formation at 700°C

Exposure of 304 samples at 700°C results in severe spalling, as shown in Fig. 14a. The average thickness of the remaining oxide scale is about $3\text{ }\mu\text{m}$, while the oxide thickness in the spalled areas is only about $0.02\text{ }\mu\text{m}$. This shows that the spalling takes place during cool down. Otherwise

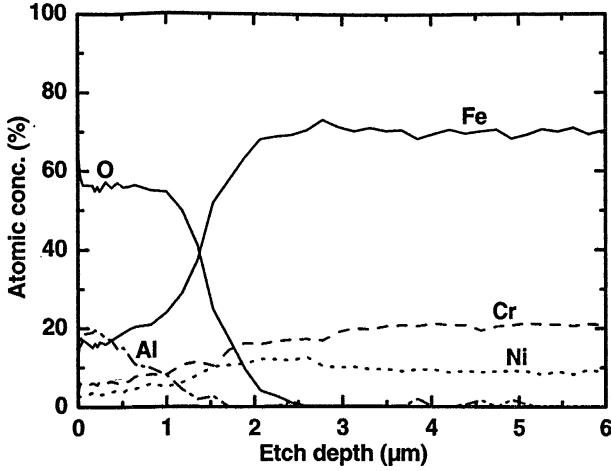


Fig. 11. AES depth profiles recorded from a 304 sample eroded at 550°C.

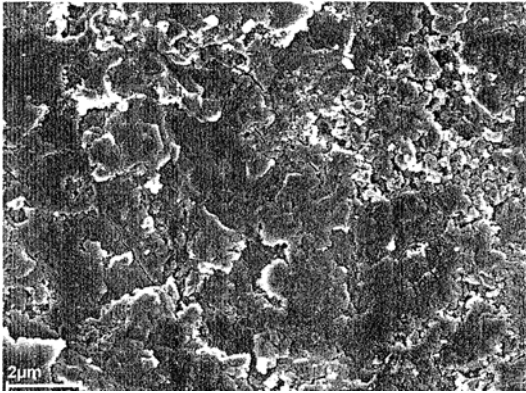


Fig. 12. SEM micrograph recorded from a 304 sample eroded at 550°C showing the presence of cracks in the oxide scale.

oxide growth would have occurred in the spalled areas. A micrograph of the remaining scale is given in Fig. 14b. The scale composition is two thirds Fe-oxide and the rest equal amounts of Cr- and Ni-oxide (Fig. 15a). Only minor amounts of alumina fragments are present and they are found solely in the outer part of the oxide. Nickel is enriched at the oxide/metal interface. AES depth profiles recorded at the corresponding non-eroded

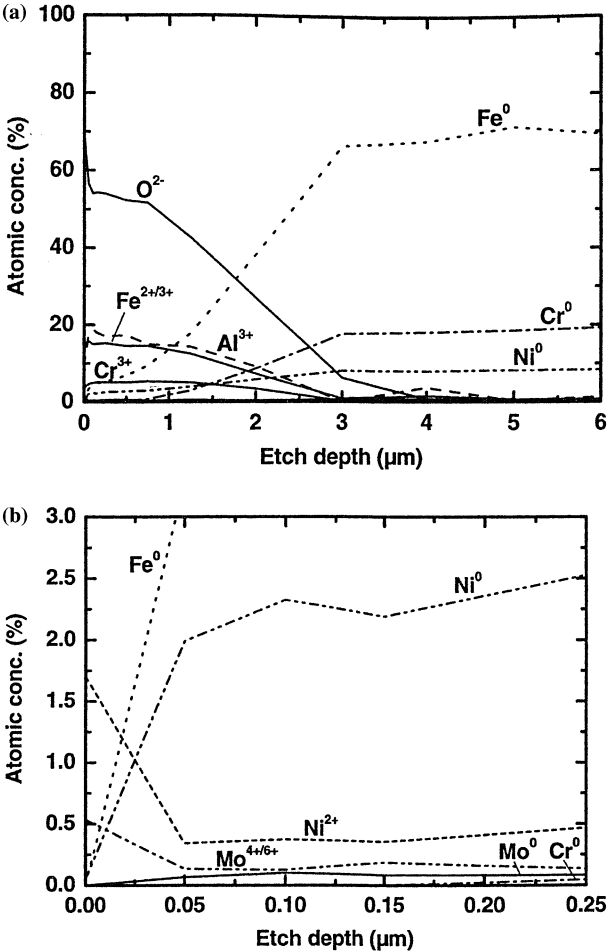


Fig. 13. XPS depth profiles recorded from a 304 sample eroded at 550°C. A close-up of the lower left-hand corner of (a) is given in (b).

area (Fig. 15b), show that the present oxide is thin, about 0.4 μm, and greatly enriched in Cr and Mn.

The structure of the oxide formed on Fe9Cr1Mo under erosion–corrosion conditions is almost identical to that on 304. Depth profiling (Fig. 16a), reveals a composition close to the bulk alloy. The oxide on the non-eroded area is thinner and somewhat enriched in Cr and Mn (Fig 16b).

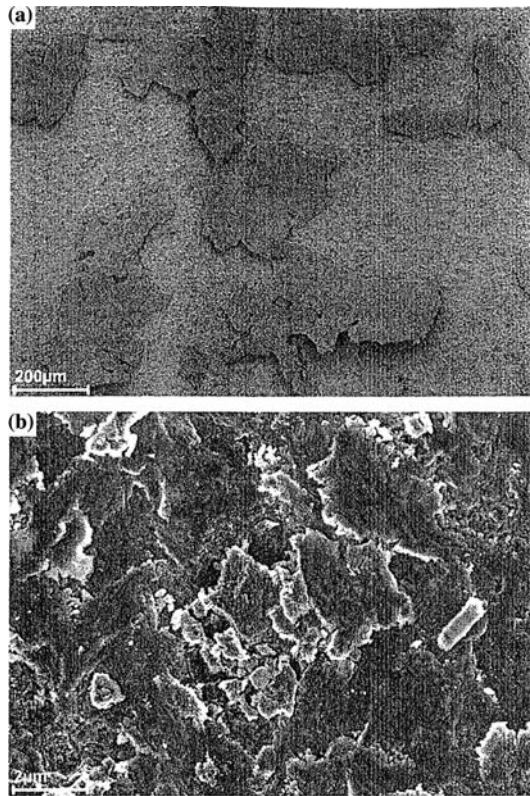


Fig. 14. SEM micrographs recorded from a 304 sample eroded at 700°C. (a) Overview of the partially spalled oxide scale, (b) the structure of the remaining oxide.

The Inconel 625 alloy displays a change in oxidation behavior when the exposure temperature is increased from 550 to 700°C. At the lower temperature a composite layer of metal oxides, bulk metal and alumina fragments is formed. Increasing the temperature gives Ni and Cr oxides underneath a deposit layer of alumina fragments, as shown by the depth profiles in Fig. 17a. The oxide on the non-eroded area is almost pure chromia (Fig. 17b).

Table III gives a complete summary of the surface layer thicknesses at the different exposure temperatures as recorded by AES depth profiling. Each value is an average calculated from several measurement points. The standard deviations therefore represent the variation in thickness over the respective surfaces. The alumina fragments have been included in the

Table III. Average surface layer thicknesses measured by AES depth profiling

Thickness (μm)	Erosion–corrosion				Pure oxidation		
	20°C	350°C	550°C	700°C	350°C	550°C	700°C
Fe2.25Cr1Mo	1.3±0.4	4.2±1.2	4.9±1.7	–	0.4±0.2	30±10 ^a	–
Fe9Cr1Mo	1.3±0.2	2.4±1.1	1.9±0.9	3.5±0.3	0.09±0.01	0.30±0.15	0.8±0.3
AISI 304	1.3±0.2	3.2±0.8	1.3±0.4	3.4±0.5 ^b	0.023±0.001	0.04±0.01	0.4±0.2
353 MA	1.2±0.2	2.7±0.9	2.0±0.5	2.0±0.3	0.015±0.001	0.12±0.02	0.7±0.2
Inconel 625	1.0±0.2	4.3±1.5	0.9±0.2	0.7±0.1	0.019±0.001	0.17±0.10	0.3±0.1

^aTotal spalling: thickness mechanically measured on spalled flakes.

^bPartial spalling: depth profiling performed on adherent flakes.

calculations as they are intermixed with the oxide. It appears that except for the Fe2.25Cr1Mo alloy at 550°C, the surface layers developed on the eroded areas are much thicker than those formed by pure oxidation. As expected, the oxide thickness during pure oxidation increases with exposure temperature for all the alloys. However, on the eroded areas the surface layer thickness recorded at 350°C is generally larger than that at 550°C, reflecting extensive incorporation of alumina fragments.

DISCUSSION

In this study a minimum in erosion–corrosion wastage rate is exhibited at about 350°C by the investigated ferritic steels and Ni-based superalloy, when exposed to a dilute stream of erodent at a low velocity. The austenitic steels show almost equal wastage rates at room temperature and at 350°C. Exposure at 700°C results in a dramatic increase in wastage rate for two of the tested materials; in comparison to 550°C it is six times higher for the ferritic steel Fe9Cr1Mo and thirteen times higher for the austenitic superalloy Inconel 625. On the other hand, the austenitic steels 304 and 353 MA show only a twofold increase. A similar temperature dependence but with a minimum wastage at 450°C was observed by Stringer and co-workers¹⁴ for 1018 steel. However, the experimental conditions are rather different in their case since the samples were actuated up and down in a hammering motion, at an approximate velocity of 1 m/s, inside a fluidized bed. In commercial FBC power plants the wastage rate is usually radically decreased when the temperature exceeds 400°C. This is often attributed to the formation of a protective oxide scale, but may also involve deposition of bed material on the metal surface.¹⁹ Protection by deposits is shown to be particularly important, when the bed material contains any of the following calcium compounds: limestone, CaCO₃; calcined limestone, CaO; or reacted limestone, CaSO₄.²⁰

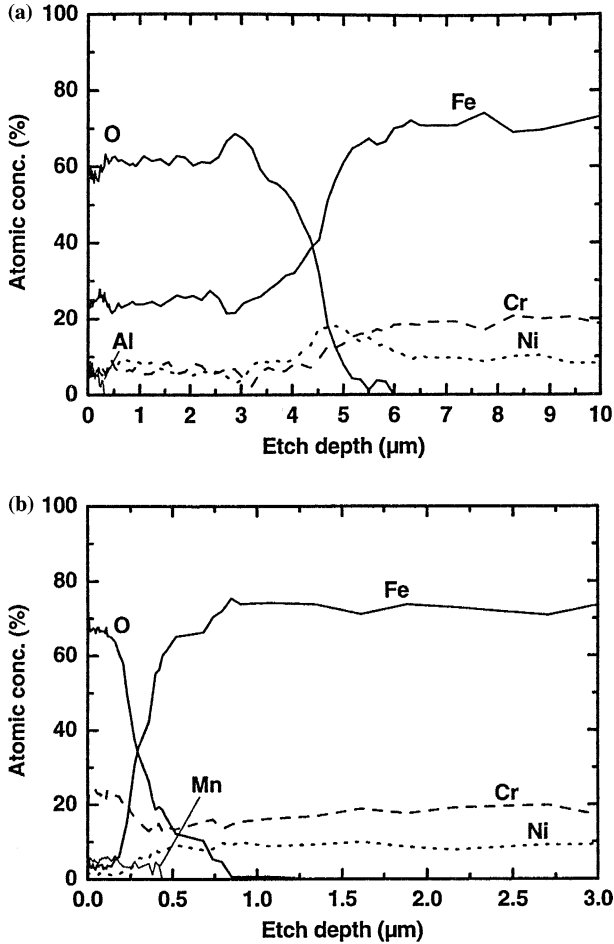


Fig. 15. AES depth profiles recorded from a 304 sample exposed at 700°C. (a) Eroded area, (b) area subjected to pure oxidation.

The wastage rate is related to the surface chemistry and morphology developed in the erosion-corrosion regime at the temperature in question. According to the nomenclature of Rishel *et al.*,⁹ a number of different regimes can be identified in the present case. At room temperature, all materials exhibit erosion of metal only. The oxidation rate becomes significant when the temperature is increased. The presence of oxides formed from the alloys at 350°C shows that a transition to the oxidation-affected erosion regime has occurred. The eroded scale on the steels at 550 and

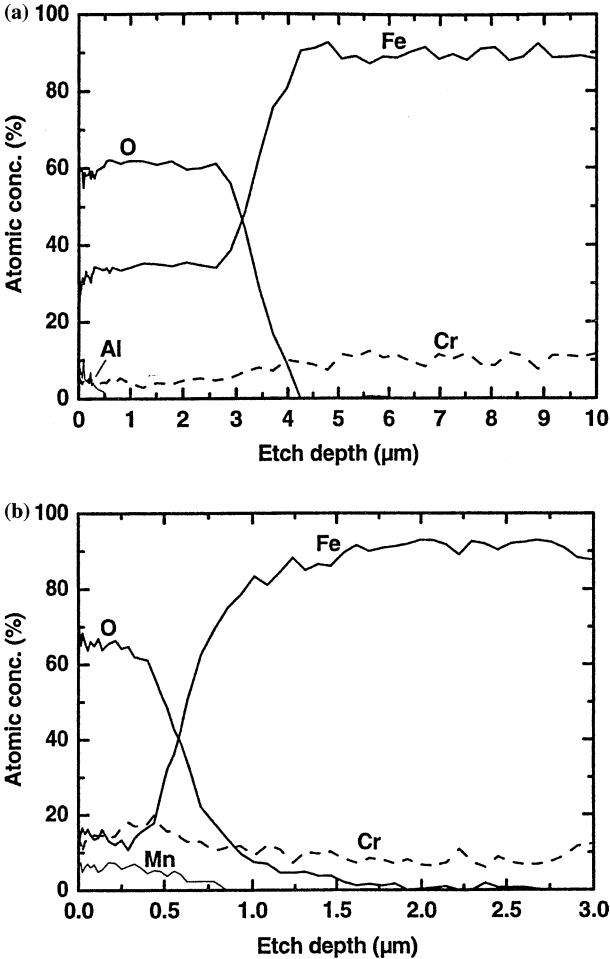


Fig. 16. AES depth profiles recorded from an Fe9Cr1Mo sample exposed at 700°C. (a) Eroded area, (b) area subjected to pure oxidation.

700°C grows to a larger thickness than the one formed by pure oxidation for the same time. Thus this regime is erosion-enhanced corrosion type II. It has been shown previously¹⁵ that cracks and channels are induced in the oxide scale during particle bombardment. This allows for molecular oxygen access to the oxide/metal interface and an enhanced oxidation rate. The oxide cation concentration will be close to that of the bulk, while the elements with the strongest oxygen affinity are usually enriched in the

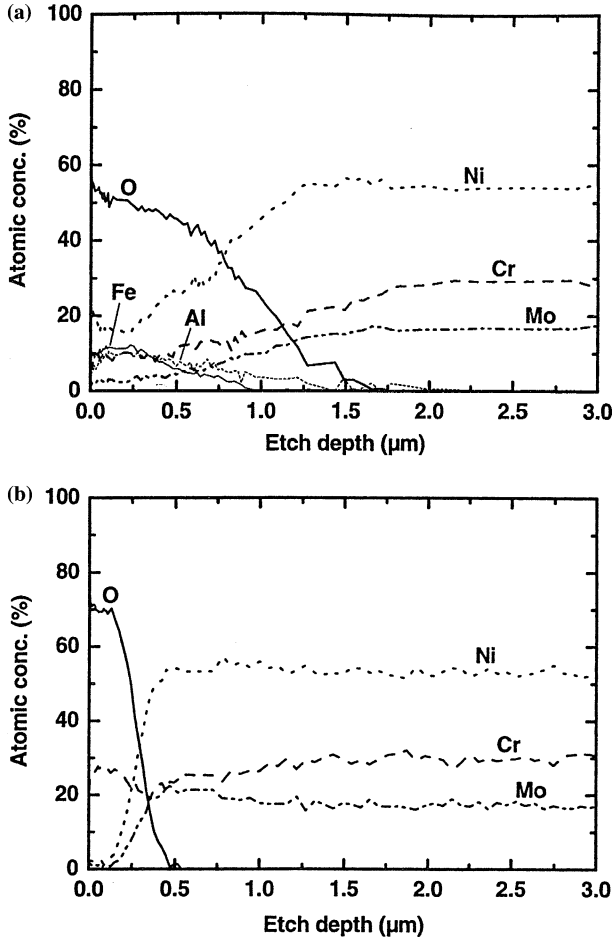


Fig. 17. AES depth profiles from an Inconel 625 sample exposed at 700°C. (a) Eroded area, (b) area subjected to pure oxidation.

oxide on the non-eroded area. The nickel based superalloy **Inconel 625** oxidizes more slowly and it is required that the temperature be raised to 700°C for a transition into the regime erosion-enhanced corrosion type II.

The degradation mechanism at room temperature is obviously erosive wear of the metal directly, though the wear resistance is probably improved by the large surface coverage of hard alumina fragments. At 350°C the oxidation rate is rather low and particle bombardment results in the formation of a composite surface layer consisting of alumina

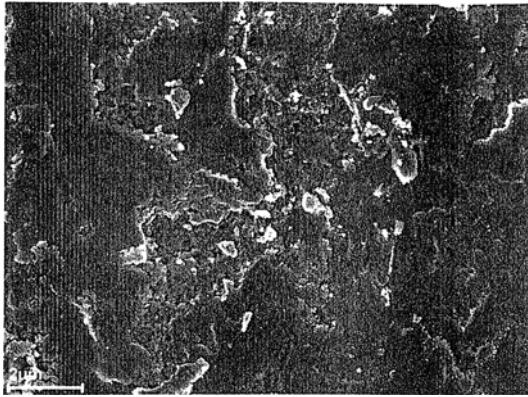


Fig. 18. SEM micrograph recorded from an Fe9Cr1Mo sample eroded at 700°C.

fragments incorporated into a mixture of base metal and its oxides. The wear resistance of the surface is increased by toughening from particle strengthening of alumina fragments in the composite surface layer and the wastage rate becomes low. In the erosion-enhanced corrosion regime developed on steels at 550°C chipping of oxide fragments from the outer part of the oxide scale appears to be the primary cause of material loss. The statement is supported by the observation that alumina fragments penetrate deep into the oxide scale. Thus chipping of oxide fragments and crack formation are most likely to occur. The amount of alumina fragments present in the oxide scale decreases with increasing temperature. At 700°C the amount of incorporated alumina on the steels is close to negligible and less chipping and crack formation is expected. Nevertheless, some cracks and channels are observed allowing for enhanced oxidation also at this temperature. Due to the high temperature the metal phase is rapidly oxidized. Oxide formation at the bottom of a crack leads to a local expansion of the scale at that site and the overlaying oxide is pushed outwards. This protruding oxide flake is either immediately broken off, due to the growth stresses, or chipped by a later impact. Evidence of this mechanism is shown in Fig. 18, where a chipped oxide flake exposes the sponge-like oxide rapidly grown at the oxide/metal-interface. It is suggested that the dramatic increase in wastage rate on the Fe9Cr1Mo and 304 alloys reflects the larger degree of chipping of protruding oxide flakes. Some indication of this phenomenon is observed also on Inconel 625 exposed at the same temperature. However, the corresponding increase in wastage rate may also reflect a gradual transition into the erosion-enhanced regime, as

indicated by the AES depth profiles. The increased wastage rate is a result of less particle strengthening in this regime.

The 304 material spalls during cool-down from 700°C. Since no spalling takes place at the exposure temperature, this alloy is classified as being in the type II erosion-enhanced corrosion regime and not in the more severe type III regime. In practical use at higher temperatures this alloy will probably be very sensitive to environmental variations, such as temperature fluctuations, which may trigger spalling and thus increase the wastage rate dramatically. The 353 MA material shows similar in-depth oxide composition as the 304 material, but the stronger oxide adhesion preventing spalling on this alloy is usually considered a result of the Ce addition.²¹

Although the combustion environment in commercial FBC power plants differs radically from the environment used in this study, some general findings can be noted. All materials, except Fe2.25Cr1Mo, appear usable at metal temperatures up to 550°C. Fe9Cr1Mo and Inconel 625 become inapplicable at 700°C, due to their high wastage rates. The wastage rate on the 304 alloy is much lower, but its susceptibility to spalling makes it unsuitable. Thus, only 353 MA is likely to perform well at the highest temperature. However, it must be mentioned that metal temperatures as high as 700°C are still quite unusual in FBC power plants and at these temperatures also creep strength must be taken into consideration.

CONCLUSIONS

Four steels (Fe2.25Cr1Mo, Fe9Cr1Mo, AISI 304, 353 MA) and one Ni-based superalloy (Inconel 625) have been exposed to an alumina erodent in an erosion-corrosion test rig at the temperatures 20, 350, 550 and 700°C. The conclusions are as follows:

- The largest erosion-corrosion resistance is obtained when a particle strengthened composite layer consisting of erodent fragments, metal oxide and base metal is formed on the surface.
- The regime transition from oxidation-affected erosion to erosion-enhanced corrosion increases the wastage rate.
- The compositions of the oxides formed in steady-state erosion-corrosion, reflect the compositions of the alloy.
- The erosive process at intermediate temperatures is chipping of small oxide fragments from the surface of the oxide.
- At the highest temperature the Fe9Cr1Mo, AISI 304 and Inconel 625 alloys are degraded by chipping of protruding oxide flakes. This is induced by a push-out effect caused by the growth of oxide nodules

formed from the metal exposed at the bottom of the cracks induced by the particle bombardment.

- The amount of fragments from the alumina erodent incorporated in the oxide decreases with increasing temperature.

ACKNOWLEDGMENTS

This work was performed in the Swedish High-Temperature Corrosion Center (HTC) which is acknowledged for financial support. Avesta Polarit AB, Kvaerner Pulpung AB and Vattenfall Utveckling AB are acknowledged for supplying the materials.

REFERENCES

1. N. Henriksen, and O. H. Larsen, *Materials at High Temperatures* **14**, 157 (1997).
2. J. Stringer, *Wear* **186–187**, 11 (1995).
3. G. Sundararajan, *Proceedings of the Corrosion–Erosion–Wear of Materials at Elevated Temperatures* (NACE Int., Houston, TX, 1990), pp. 11.1–11.33.
4. D. J. Stephenson, and J. R. Nicholls, *Corrosion Science* **35**, 1015 (1993).
5. I. G. Wright, V. K. Sethi, and A. J. Markworth, *Wear* **186–187**, 230 (1995).
6. C. T. Kang, F. S. Pettit, and N. Birks, *Metallurgical Transactions A* **18**, 1785 (1987).
7. M. M. Stack, F. H. Stott, and G. C. Wood, *Wear* **162–164**, 706 (1993).
8. S. Hogmark, Å. Hammarsten, and S. Söderberg, *Proceedings of the 6th International Conference on Erosion by Liquid and Solid Impact* (Cambridge, UK, 1983), paper 37.
9. D. M. Rishel, F. S. Pettit, and N. Birks, *Materials Science and Engineering A* **143**, 197 (1991).
10. F. H. Stott, S. W. Green, and G. C. Wood, *Materials Science and Engineering A* **120–121**, 611 (1989).
11. V. K. Sethi, and R. G. Corey, *Proceedings of the 7th International Conference on Erosion by Liquid and Solid Impact* (Cambridge, UK, 1987), paper 73.
12. A. J. Ninham, I. M. Hutchings, and J. A. Little, *Corrosion* **46**, 296 (1990).
13. B. Q. Wang, G. Q. Geng, and A. V. Levy, *Wear* **159**, 233 (1992).
14. S. S. MacAdam, and J. Stringer, *Corrosion* **49**, 156 (1992).
15. R. Norling, and I. Olefjord, *Wear* **254**, 173 (2003).
16. H. Asteman, R. Norling, J.-E. Svensson, A. Nylund, and L. Nyborg, *Surface and Interface Analysis* **34**, 234 (2002).
17. I. Finnie, and D. H. McFadden, *Wear* **48**, 181 (1978).
18. I. Finnie, *Wear* **186–187**, 1 (1995).
19. J. Stringer, S. S. MacAdam, I. G. Wright, and V. K. Sethi, *Journal de Physique IV* **3**, C9, 797 (1993).
20. A. V. Levy, *Corrosion Science* **35**, 1035 (1993).
21. A. S. Khanna, *Introduction to High Temperature Oxidation and Corrosion* (ASM Int., Materials Park, OH, 2002), Ch. 11.